scientific reports



OPEN

Single-shot wavelength-multiplexed phase microscopy under Gabor regime in a regular microscope embodiment

Vicente Micó^{1⊠}, Mikołaj Rogalski², José Ángel Picazo-Bueno¹ & Maciej Trusiak²

Phase imaging microscopy under Gabor regime has been recently reported as an extremely simple, low cost and compact way to update a standard bright-field microscope with coherent sensing capabilities. By inserting coherent illumination in the microscope embodiment and producing a small defocus distance of the sample at the input plane, the digital sensor records an in-line Gabor hologram of the target sample, which is then numerically post-processed to finally achieve the sample's quantitative phase information. However, the retrieved phase distribution is affected by the two well-known drawbacks when dealing with Gabor's regime, that is, coherent noise and twin image disturbances. Here, we present a single-shot technique based on wavelength multiplexing for mitigating these two effects. A multi-illumination laser source (including 3 diode lasers) illuminates the sample and a color digital sensor (conventional RGB color camera) is used to record the wavelength-multiplexed Gabor hologram in a single exposure. The technique is completed by presenting a novel algorithm based on a modified Gerchberg-Saxton kernel to finally retrieve an enhanced quantitative phase image of the sample, enhanced in terms of coherent noise removal and twin image minimization. Experimental validations are performed in a regular Olympus BX-60 upright microscope using a 20X 0.46NA objective lens and considering static (resolution test targets) and dynamic (living spermatozoa) phase samples.

Abbreviations

SD

QPI Quantitative phase imaging DHM Digital holographic microscopy TIE Transport of intensity equation AS Angular spectrum **RGB** Red-green-blue G-S Gerchberg-Saxton FOV Field of view **USAF** United State Air Force **CFF** Complex filed filtration

Standard deviation

Quantitative phase imaging (QPI) is a microscopy discipline aimed to quantify the phase delays happening when light passes through a sample having a spatially variant density distribution^{1,2}. Although not being the unique option³, digital holographic microscopy (DHM) is doubtlessly the most common technique to achieve QPI, particularly in biological research^{4,5} and industrial applications^{6,7}.

Building a simple arrangement is of particular significance in DHM since it provides a compact and costeffective solution in a comprehensive and easy-to-use way for QPI. Thus, DHM has been proposed using a single

¹Departamento de Óptica y Optometría y Ciencias de la Visión, Universidad de Valencia, C/Doctor Moliner 50, 46100 Burjassot, Spain. ²Institute of Micromechanics and Photonics, Warsaw University of Technology, 8 Sw. A. Boboli St., 02-525 Warsaw, Poland. [⊠]email: vicente.mico@uv.es

interferometric element such as a thick glass plate⁸, a wedge prism⁹, a Fresnel's biprism¹⁰, a Lloyd's mirror¹¹, a beam splitter cube¹² or a diffraction grating¹³, just to cite some examples. Also following in this uncomplicated and compact way to produce QPI, several attempts have been dedicated to convert—with minimal modifications—a regular white light microscope into a microscope with coherence sensing capabilities. Some proposals successfully adapt an external add-on module to the exit port of a regular microscope such as, for instance, modules based on wavefront sensing¹⁴, Michelson-based layouts^{15,16}, lateral shearing interferometers^{17,18}, transport of intensity equation (TIE) algorithms^{19,20}, diffraction phase microscopy²¹, beam splitter interferometer²² or purely numerical kernel²³.

Going deeper into this simplicity path, probably the easiest way to provide holographic recording is by using the Gabor's principle of holography²⁴ by incorporating a coherent illumination source in a regular microscope embodiment and by introducing a small defocus at the sample plane. The recorded defocused image can be considered as a digital Gabor in-line hologram, where the magnification is not coming from the geometrical projection of the sample at the recording plane—as in the classical lensless geometry—but introduced by the microscope embodiment itself. Imaging is then achieved by digital refocus to the best image plane using well-known numerical propagation algorithms²⁵. Maybe the strongest limitation of this methodology is the restriction imposed by the Gabor's regime, that is, the sample must be weakly diffractive or, in other words, the amount of light blocked/diffracted by the sample should be a small fraction in comparison with the one passing without being perturbed by the sample^{26,27}. Nevertheless, there is a wide range of biological samples (single cell analysis, thin structured samples, sparse biosamples, etc.) matching the Gabor's condition, thus opening a huge potential for the application of this methodology.

Surprisingly, this extremely simple way to produce QPI in microscopy is relatively new²⁸⁻³¹. Mandula et al. derived phase from defocus²⁸ as a simple and compact phase imaging microscope for long-term observation of non-absorbing biological samples as well as its combination with fluorescence microscopy in a single dual-mode imaging platform using a standard bright-field objective²⁹. A similar concept for combining fluorescence with phase microscopy was reported by de Kernier et al.³⁰. And Micó et al. recently reported on an extremely simple, low cost and compact way to update a standard bright-field microscope with coherent sensing capabilities³¹. In their work³¹, the authors characterized the best axial defocusing to be applied at the sample plane when considering a 20× microscope lens to retrieve full quantitative phase information after the numerical processing stage based on angular spectrum (AS) algorithm. But the main drawbacks in that configuration from a QPI point of view are the same that the presented ones in Gabor's holography concept: the coherent noise (interference patterns coming from back reflections, coherent artefacts, non-uniformities, speckles, etc.) and the twin image problem that introduce phase disturbances in the retrieved QPI values as a direct consequence of using coherent illumination in an in-line holographic arrangement.

To mitigate all those problems, we present here a wavelength multiplexing approach where 3 wavelength-coded digital holograms are recorded in a single snapshot of a color camera, thus allowing fast events analysis coming from living samples. RGB illumination (using 3 fiber coupled laser diodes) is used to transmit in parallel 3 Gabor holograms and a color digital camera records the multiplexed hologram, from which the 3 wavelength-coded in-line holograms can be extracted. Once separated, the information included within each color-coded channel is numerically processed using a novel algorithm based on a modified Gerchberg–Saxton (G–S)³² kernel aided with object plane constraints³³ to provide improved QPI of the sample, improved in terms of coherent noise removal and twin image minimization.

Similar approaches based on wavelength multiplexing have been proposed in the field of lensless imaging^{34–45}. Noom et al. presented a quantitative phase contrast lensless holographic microscope first under sequential illumination/recording³⁴ and later with high-speed capabilities³⁵. Sanz et al. also reported on a novel concept of a compact, cost-effective and field-portable lensless microscope³⁶ based on wavelength multiplexing and a fast and robust algorithm for twin image minimization and noise reduction³⁷. They also extended such concept to a lensless imaging platform with different resolutions/magnifications³⁸ and considering 4 multiplexing channels³⁹. Kazemzadeh et al. proposed the use of pulsed illumination to even expand up to 5 channels and developed a multispectral lens-free microscope for biological specimens⁴⁰. Liu et al.⁴¹ and Guo et al.⁴² reported on the use of a rotating filter wheel as key concept to provide multiple wavelength illuminations onto the sample in the field of lensless imaging for improving autofocusing⁴¹ and for noise reduction⁴². Luo et al. proposed a wavelength scanning method for pixel superresolution⁴³. Liu et al. recently proposed the use of field of view (FOV) multiplexing for allowing single-shot operational principle in multi-illumination lensless imaging⁴⁴. And Zuo et al. demonstrated lensless quantitative phase microscopy and diffraction tomography based on a compact on-chip platform based on multi-wavelength phase retrieval and multi-angle illumination diffraction tomography⁴⁵.

However, the concept of wavelength multiplexing for image quality improvement working with regular microscopes has not been previously reported to the best of our knowledge. Closely related to the proposed concept is the work proposed by Waller et al. to retrieve phase information based on a transport of intensity (TIE) algorithm, where the axial defocus needed between images is provided by the intrinsic chromatic aberration of the microscope lenses⁴⁶. They used broadband illumination and conventional RGB color camera for providing 3 slightly defocused images (in-focus, and under and over focus) corresponding with the 3 color camera channels and those 3 intensity images were the inputs of the TIE algorithm. Although aimed in the same direction (improve QPI in a single-shot by reducing coherent noise), Waller et al. work is conceptually different to our proposed method. Moreover, it is penalized by the low-frequency noise presented in TIE-based phase reconstructions and it depends on the amount of chromatic aberration introduced by the objective lens, something that must be somehow calibrated before applying TIE recovery.

Experimental methodology

Figure 1 includes a scheme of the experimental layout where the proposed approach has been implemented and validated. It represents a regular upright microscope embodiment (Olympus BX-60 with UMPlanFl 20× 0.46NA objective) where a fiber coupled laser source (Blue Sky Research, SpectraTec 4 STEC4 405/450/532/635 nm) is externally inserted to provide coherent illumination in the system. Essentially, the arrangement is the same as in Ref. 31 but here we use multi-wavelength simultaneous illumination (450/532/635 nm) instead of a single emitter (as used in Ref.³¹) to provide the 3 color-coded holograms in parallel and a color camera (Ximea USB3 MQ042CG-CM, CMOS sensor type, 2048 × 2048 pixels, 5.5 µm pixel pitch, 90 fps) instead of a monochrome one (as in Ref.³¹) for decoding the 3 transmitted in-line holograms from a single snapshot. In the proposed setup, the defocus distance Δz (see Fig. 1) is one of the key factors and must be properly defined. This value was set experimentally in Ref. 31 by analyzing 2 different metrics: resolution of the reconstructed USAF test target images and standard deviation (SD) of a background (object free) area. Since we are using here the same layout as in Ref. 31, the same experimental conditions prevail so the defocusing distance is set to $\Delta z = 90 \, \mu \text{m}$, meaning that the sample is moved away 90 µm from the typical objective working distance. For setups with different parameters (including objective's NA and magnification, camera characteristics and focal lengths of tube lens), different Δz values will be optimal. Up to the best of our knowledge, no theoretical solution has been proposed for setting optimal Δz distance as a function of the microscope parameters. Therefore, for different arrangements, we propose to repeat Δz calibration process described in Ref. 31.

Figure 2 shows the diagram of our iterative algorithm processing patch and Fig. 3 presents the propagated optical field during first 4 steps of the algorithm when considering an USAF phase resolution test target. In the first step of the first iteration (n = 1), the optical field at the hologram plane (C_1) is assumed to be equal to the square root of the blue wavelength hologram (H_B) —Fig. 3b. Then, it is backpropagated a distance $-\Delta z'$ to the object plane with the angular spectrum $(AS)^{47}$ method and considering the blue wavelength illumination (λ_B) —Fig. 3a and c. Notice that $\Delta z'$ will be the same for each wavelength when considering achromatic systems. After that, both real and imaginary parts of the optical field (S_1) are processed with a novel complex field filtration (CFF) algorithm, which is partially based on a halo removal method presented in Ref. 42. CFF algorithm for the real part of S_1 (Re $\{S_1\}$) is described with equations below:

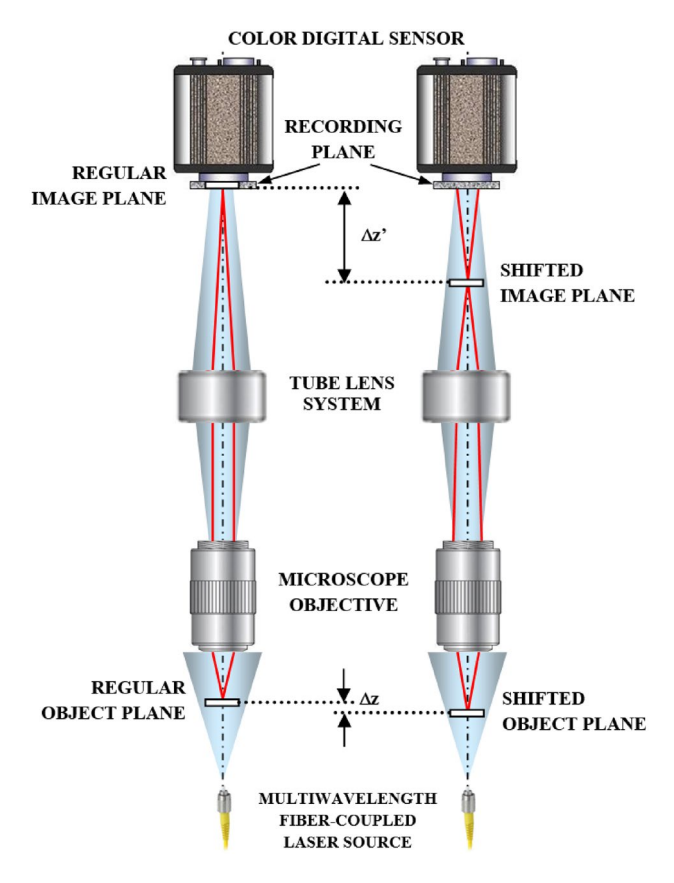


Figure 1. Optical scheme of the proposed approach. The sample is slightly shifted (Δz) from its regular object plane position (left vertical drawing) allowing to shift the conjugated image plane $(\Delta z')$ for the digital recording of an in-line hologram (right vertical drawing).

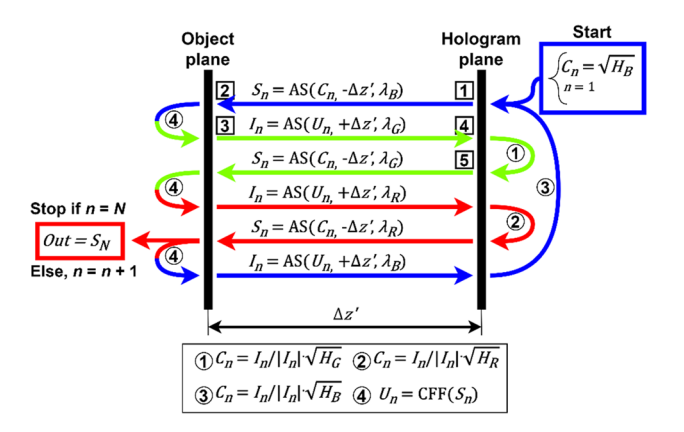


Figure 2. Diagram of the proposed algorithm processing path. Hi represents the hologram recorded with i (R, G or B) wavelength illuminations. Numbers from 1 to 5 in square frames correspond to images in Fig. 3 marked with the same numbers.

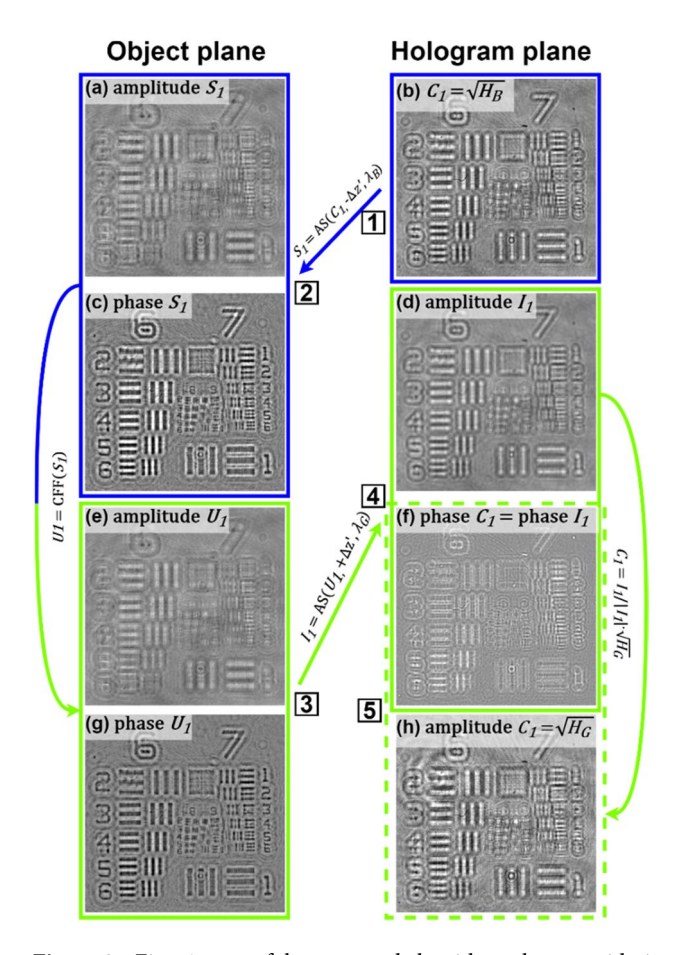


Figure 3. First 4 steps of the proposed algorithm when considering an USAF phase resolution test target. Numbers from 1 to 5 in square frames correspond to parts of the algorithm in the diagram of Fig. 2 marked with the same numbers.

$$J_{blr}(r) = \operatorname{Re}\{S_1(r)\} * w(r) \tag{1}$$

$$J_{flt}(r) = \text{Re}\{S_1(r)\}, \quad \text{if } \text{Re}\{S_1(r)\} \ge J_{blr}(r)$$

$$J_{flt}(r) = \frac{\text{Re}\{S_1(r)\} + J_{blr}(r)}{2}, \quad \text{if } \text{Re}\{S_1(r)\} < J_{blr}(r)$$
(2)

where r stands for spatial coordinates in object plane, w is a gaussian kernel (standard deviation equal 60 and filter dimensions equal 241×241 pixels), * stands for convolution operation, J_{blr} is a blurred image and J_{fit} is a filtered

image. It is worth to underline that the conditions in Eq. (2) are checked for each pixel separately. The imaginary part of S_1 is filtered similarly as the real one (with the same gaussian kernel). The resulting optical field after CFF algorithm (U_1) —Fig. 3eand g—is then propagated to the hologram plane at $+\Delta z'$ distance considering in this case the green wavelength (λ_G)—Fig. 3d and f. At the hologram plane, the optical field (I_1) is updated by replacing its amplitude part by the square root of the hologram recorded with green illumination (H_G) , while its phase factor remains unchanged - Fig. 3f and h, defining an updated C_1 . Then, this updated C_1 is further processed, according to the diagram presented in Fig. 2 and considering G (and later G) wavelength illumination. First (or each) iteration finishes with G_n backpropagated to the object plane considering the G0 wavelength illumination (bottom-left part of the diagram in Fig. 2). The algorithm is computed for the user-specified number of iterations G1. Figure 4 shows the exemplary USAF phase test target reconstructions with different number of iterations and Fig. 4f shows the plot of the root mean square (RMS) value of the difference between phase reconstruction in G1 iteration. As can be observed, after several first iterations, there is a significant improvement in the reconstruction resolute, but after that (since around 5th iteration), the algorithm converges and there is not much difference between the results. Therefore, we usually set G1 is sufficient to obtain good quality results, without unnecessary increasing the reconstruction time.

Results

Figure 5 presents the exemplary reconstructions of the USAF phase resolution test target, comparing various methods. Figure 5a shows the intensity distribution in the in-focus position for the blue wavelength. As the imaged target is transparent, registered image is of very low contrast. Figure 5b presents the phase result of a blue hologram backpropagated with the AS method to the object plane and Fig. 5c shows the AS result filtered with CFF algorithm. Figure 5d and e show the G–S reconstructions without CFF considering 2 (GB) and 3 (RGB) simultaneous wavelengths. G–S reconstructions with CFF for 1 (B), 2 (GB) and 3 (RGB) wavelengths are shown in Fig. 5f–h respectively. Comparing simple AS backpropagation with G–S algorithm, the twin image effect is significantly reduced for G–S, especially for the 3 simultaneous wavelengths case. However, it is still observable, similarly to a "halo" effect (white pixels in Fig. 5d,e). After applying CFF, this "halo-like" effect is almost completely extinguished. Comparing the G–S+CFF reconstructions with single and multi-wavelength cases, single-wavelength case, Fig. 5f, contain significantly higher number of twin-image artifacts ("fake" negative values in the image background) than 2 and 3 wavelength cases, Fig. 5g and h.

Comparing 2 and 3 wavelengths, RGB result seems to be noticeably more robust in terms of coherent noise artifacts removal (compare top left part of FOV in Fig. 5e,f). Given the fact that recording 3 holograms (RGB) has the same level of complexity as recording 2 holograms (GB) with a RGB camera, the 3-wavelength reconstruction provides better outcomes. Cross-sections through Element 6 of Group 6 (E6-G6) of the chosen reconstructed phases are included in Fig. 5i. In the no-CFF reconstructions, some "fake" positive phase values can be observed (marked with red dashed ellipses) in object-free regions, which are only visible on a small scale in CFF cross-sections. When comparing G-S+CFF reconstruction with single and three illuminations, again "fake" negative phase values are observable for single-wavelength case [marked with black arrow in Fig. 5i].

Figure 6 includes a standard deviation (SD) analysis of the background for all the compared reconstructions. Figure 6a presents all the SD background values in a table while Fig. 6b shows the region (black rectangle) where the SD values are computed and the full FOV phase image (AS backpropagated with B wavelength illumination) from which the region of interest (red rectangle) is included in Fig. 5. As expected, there is a SD reduction when

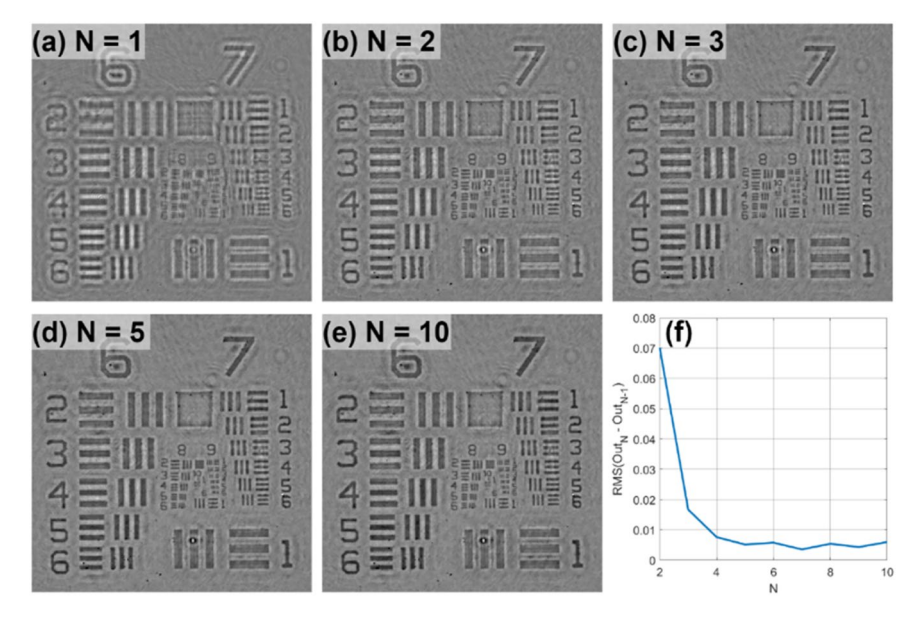


Figure 4. (a)–(e) Reconstruction of USAF phase test target for a different number of iterations (N). (f) RMS of the difference between N and N - 1 iteration results.

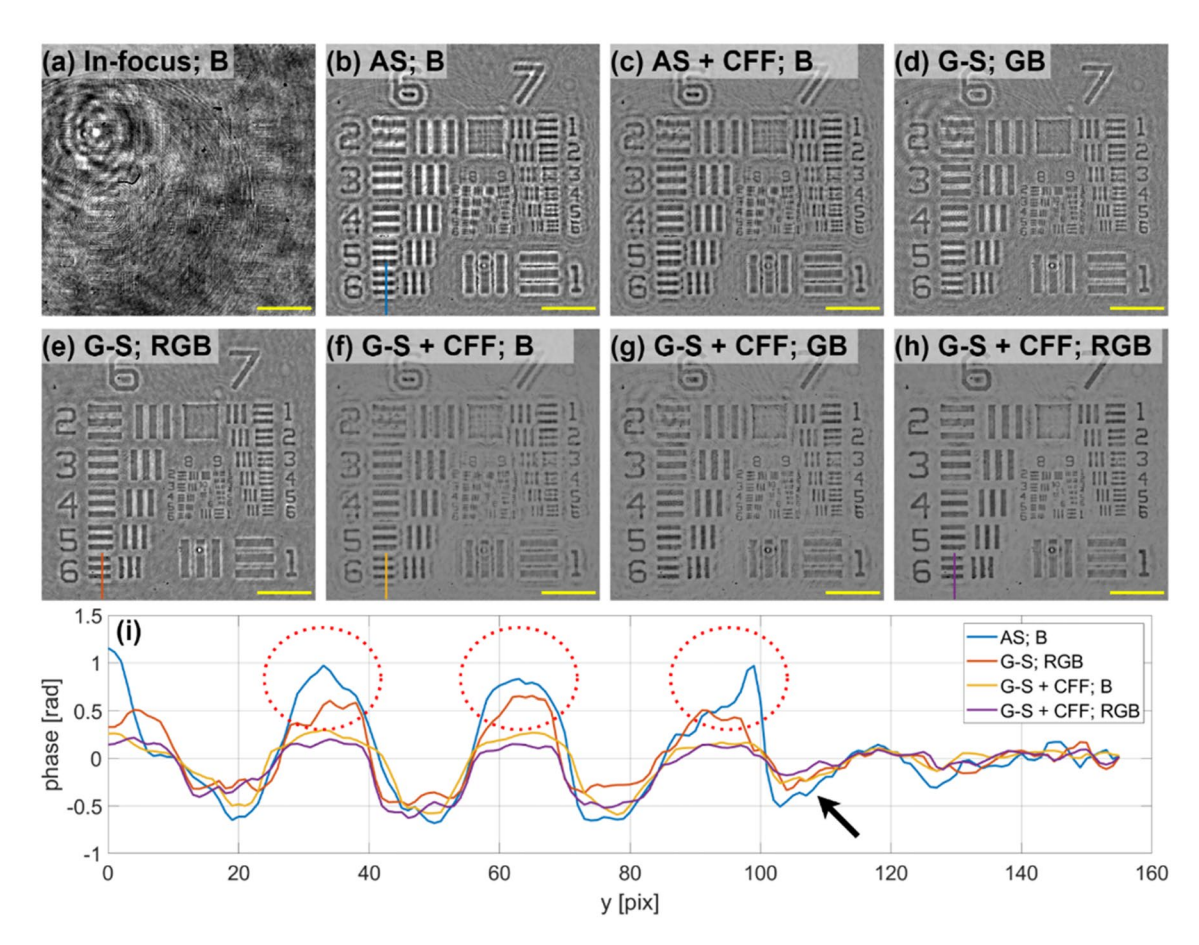


Figure 5. Experimental comparison of different phase reconstruction methods for the case of an USAF phase test target. (a) In-focus intensity image considering the blue illumination, and its phase reconstructions from defocused images with: (b) AS backpropagation, (c) AS backpropagation result filtered with CFF (d) GB G–S, (e) RGB G–S, (f) B G–S+CFF, (g) GB G–S+CFF, and (h) RGB G–S+CFF methods. (i) Cross-sections through the group 6 element 6 of the reconstructed phases. Phase values for (b)–(h) are displayed in [-1,1] rad range and the yellow scale bar is 50 μm long.

(a)	SD for black area [10 ⁻² rad]	(b)
AS; B	8.2	6 7
AS + CFF; B	6.2	
G-S; GB	7.4	3=1112
G-S; RGB	6.9	
G-S + CFF; B	3.6	<u>GEM 800 CD</u>
G-S + CFF; GB	4.7	
G-S + CFF; RGB	3.9	

Figure 6. (a) Comparison of the background SD values from the reconstructions provided by the different methods. (b) Full FOV retrieved phase image with B AS where the black/red rectangles mean the area for SD calculation and the region of interest showed in Fig. 5, respectively. Yellow scale bar is 100 µm long.

including additional wavelengths and also with CFF algorithm application as consequence of the averaging, yielding in a reduction factor slightly above 2 when passing from traditional 1 wavelength reconstruction to the proposed method. The only exception is the smaller SD value for G–S+CFF reconstruction with single-wavelength illumination compared to multi-wavelength illumination cases. This is due to the high coherent noise present in G illumination hologram. Nevertheless, despite that fact, RGB reconstruction achieves only slightly larger SD than B reconstruction, which means that this G coherent noise is minimized by the proposed algorithm.

Aside of the validation performed with the static phase target and included in previous figures, maybe the most appealing feature of the proposed method relates to its capability to work in a single shot. To demonstrate this feature, we have conducted experiments using a live human sperm sample. The sperm cells have approximately a head length and width of 4 and 5 μ m, respectively, a total length of 45 μ m and a tail width below 1 μ m. The sample is placed in a counting chamber having a depth of 20 μ m (Proiser R+D, model ISASD4C20) allowing free swimming of the cells. No pre-filtering nor pre-preparation (centrifugation, dilution, re-suspension, etc.) is applied, so the sample contains a lot of additional seminal particles. Movies are recorded for 4 s at an acquisition rate of 90 fps to study the dynamic motions of the sperm cells.

Figure 7 presents the first frames of the obtained movies including the multiplexed recorded hologram—Fig. 7a, the multiplexed recorded hologram after filtering (subtracted mean recorded frame) to remove all static cells and debris—Fig. 7e, and the reconstructed phases for single wavelength backpropagation—Figs. 6f and 7b—RGB G–S without CFF—Figs. 6g and 7c—and with CFF—Fig. 7d and h. Results are presented for both no-filtration—Fig. 7b–d—and with static objects filtration—Fig. 7f–h—cases. For better clarity, phase values are unwrapped, as cells bodies have phase values below – π and the phase reconstructions are shown only for areas marked with red rectangles in Fig. 7a and e. Full FOV reconstructions for filtration free and with static objects filtration cases are presented in Visualization 1 and Visualization 2, respectively. The best results are obtained for G–S algorithm with filtration, where the spermatozoid tail may be observed (marked with a red arrow in Fig. 7g,h) For no-filtration case the spermatozoids tails are not observed, probably due to coherent noise coming from static objects. Additionally, again the smallest twin image is observed for aiding the G–S reconstruction with CFF algorithm, what results in minimizing "halo-like" effect (marked with a blue arrow in Fig. 7g) and avoiding unwrapping errors (bottom-left spermatozoid in Fig. 7f and g.

As proven above, the proposed algorithm can significantly outperform both classical G–S and AS methods in terms of quality of the reconstructed phase. However, this is achieved at a cost of increased computational complexity and therefore, increased computational time. Table 1 presents typical reconstruction times of a 2040×2040 pixels hologram on a low-cost laptop (Intel i7, 2.8 GHz CPU and Nvidia GeForce GTX 1060 GPU) for different algorithms. GPU processing was used to optimize algorithms execution time. Proposed algorithm

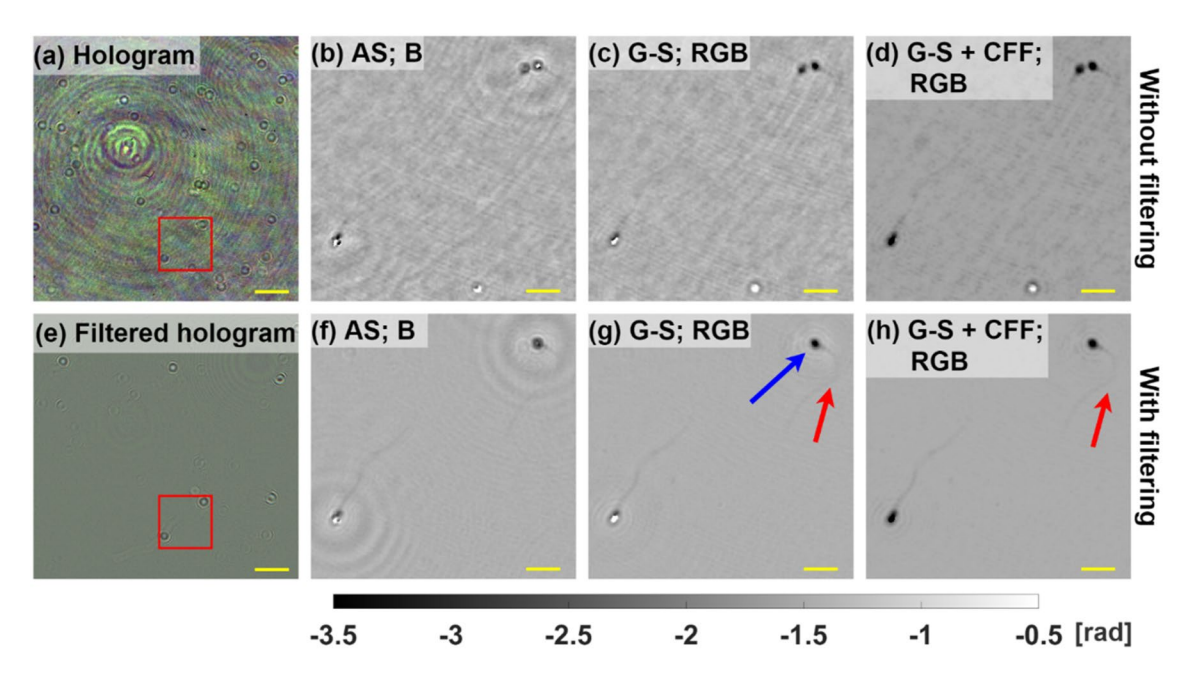


Figure 7. Experimental validation for the case of living sperm cells. Multiplexed hologram without (a) and with (e) filtration, respectively. Reconstructed phases for holograms without (b)–(d) and with (f)–(h) filtration, respectively. Yellow scale bar is 50 μ m in (a), (b) and 10 μ m in (b)–(d), (f)–(h).

Algorithm	AS	CFF	G-S; GB	G-S; RGB	G-S+CFF; B	G-S+CFF; GB	G-S+CFF; RGB
Time (s)	0.3	0.65	1.53	2.1	1.54	2.98	4.41

Table 1. Computation time of the different algorithms. G–S times are given for 5 iterations.

achieved around 15 times longer execution time than the classical AS method. However, despite that fact, below 5 s computation time for 2040×2040 holograms should still be enough for most of the applications and should not be too troublesome for the users.

Discussion and conclusions

Along this manuscript, we have presented a step forward to improve phase imaging microscopy in an upright commercially available microscope, which has been updated with coherent sensing capabilities using the simplest way one can imagine to allow holographic imaging. This is nowadays a remarkably interesting topic because it expands the use of regular microscopes for the analysis of biological samples without the need to manipulate (staining, fixing, etc.) them. Thus, it takes all the advantages provided by actual microscopes concerning image quality and stability with coherent sensing capabilities coming from digital in-line holographic microscopy. Moreover, the low cost of these type of approaches contribute to the democratization of science by allowing to perform phase imaging in biological experiments to those laboratories with constrained budget.

Through the presented images, we have experimentally shown how coherent noise and twin image are mitigated as consequence of the averaging, G–S algorithm and CFF implementation, to finally achieve an output image with improved quality. Part of this improvement is as consequence of the averaging of the 3 images during the numerical methodology but it is also coming from the CFF algorithm itself which can be understood as a way to blur out all the features that have higher amplitude ("negative absorption") and phase (smaller refractive index) values than the averaged neighboring background area while remaining unchanged all features with lower values. The phase resolution test target case clearly shows image quality improvement (twin image minimization, halolike mitigation, contrast improvement and background SD reduction). And the living sperm cells experiment shows a real biological application of the proposed approach with the same improvements in phase imaging as in the USAF target case. Here, the phase imaging enhancement allows the visualization of additional parts (full tail) of the cells, which can serve for improving the morphological analysis of the cells as well as having a better information for their 3D tracking.

As in any Gabor's implementation scheme, the main limitation concerns with the restriction imposed to the target sample (weak diffraction assumption). However, in biology and biomedicine there are plenty of cases where biosamples can be treated as weakly diffractive samples, thus satisfying the Gabor's condition and being perfect candidates to be imaged with the proposed methodology, which allows in-vivo imaging without modifying the sample environment. Moreover, Gabor's layout is commonly known by its simplicity, cost-effectiveness, compactness and aberration-free properties. But high NA values are difficult to be achieved on both classical but opposite arrangements in lensfree imaging^{48,49} due to both geometrical distortion and the mandatory compromise between the illumination pinhole diameter, the illumination wavelength, and the need to obtain a reasonable light efficiency⁴⁸ as well as because of the geometrical constraints imposed by the pixel size of the detector⁴⁹. The inclusion of a microscope objective for optically magnifying the sample while recording a defocused diffraction pattern³¹ allows to easily achieve high NA (defined by microscope objective) at the cost of a reduced FOV and the need to control aberrations. Nevertheless, this is not a significant issue in our system probably because of the in-line principle of Gabor's holography where reference and object beams travel together the same optical path and are affected by the same lenses. Moreover, since modern microscope objectives are quite well aberration balanced for the entire visible spectrum, they do not introduce any significant aberration (distortion, spherical, chromatic, etc.) that could separately affect each color-coded channel image.

Our proposed algorithm assumes ideal separation between camera spectral channels (S_i , being i=R, G, B) where only a single wavelength (λ_j , being j=R, G, B) takes contribution on each channel, that is, $S_i=\delta_{ij}\cdot f(\lambda_j)$ being δ_{ij} the Kronecker delta function. However, the presence of crosstalks on each RGB camera channel coming from the two additional wavelengths can influence in the final image quality reconstruction. Although we have not noticed any significant problem concerning this fact because the RGB selected wavelengths are close to the maximum spectral sensitivity of their corresponding camera channels, additional procedures can be defined for the case that crosstalks will be a problem. Thus, on one hand, the crosstalks can be easily removed by subtraction a set of previously recorded images using independent wavelengths³⁷ or using more complex procedures involving the definition of the wavelength detector response matrix to correct each channel reading 36,39 . Anyway, these calibration procedures must be done once and the result must be applied to each recorded frame as preliminary digital preparation of the data set before entering into the proposed workflow algorithm.

In summary, we have presented single-shot wavelength-multiplexed phase microscopy implemented in a regular microscope embodiment with minimal modifications for improving phase imaging under Gabor's regime. Validation is included for a 20X microscope objective, but it is extendable to any other lens by only defining the proper defocusing distance. Just as an application example, we have included the case of living sperm cells in a counting chamber. However, the potentiality of the proposed approach is far beyond that and it can be applied to a long list of biological cases such as, for instance, long-term observation events, including cell division and apoptosis, single cell examinations, cell to cell interactions and imaging flow cytometry.

Data availability

Data underlying the results presented in this paper are not publicly available at this time but may be obtained from the authors (maciej.trusiak@pw.edu.pl) upon reasonable request.

Received: 14 December 2022; Accepted: 9 March 2023

Published online: 14 March 2023

References

- 1. Popescu, G. Quantitative Phase Imaging of Cells and Tissues (McGraw-Hill, 2011).
- Nguyen, T. L. et al. Quantitative phase imaging: Recent advances and expanding potential in biomedicine. ACS Nano 16, 11516– 11544 (2022).
- 3. Cacace, T., Bianco, V. & Ferraro, P. Quantitative phase im-aging trends in biomedical applications. *Opt. Lasers Eng.* **135**, 106188 (2020).
- 4. Shaked, N. T., Zalevsky, Z. & Satterwhite, L. L. Biomedical Optical Phase Microscopy and Nanoscopy (Oxford Academy, 2012).
- 5. Kemper, B. et al. Label-Free Quantitative In Vitro Live Cell Imaging with Digital Holographic Microscopy Vol. 2 (Springer, 2019).
- Kreis, T. Application of digital holography for nondestructive testing and metrology: a review. IEEE Trans. Ind. Inf. 12, 240–247 (2016).
- 7. Emery, Y., Colomb, T. & Cuche, E. Metrology applications using off-axis digital holography microscopy. *J. Phys. Photon.* 3, 034016 (2021).
- Di, J. et al. Dual-wavelength common-path digital holographic microscopy for quantitative phase imaging based on lateral shearing interferometry. Appl. Opt. 55, 7287–7293 (2016).
- 9. Sun, T., Zhuo, Z., Zhang, W., Lu, J. & Lu, P. Single-shot interference microscopy using a wedged glass plate for quantitative phase imaging of biological cells. *Laser Phys.* 28, 125601 (2018).
- 10. Ebrahimi, S., Dashtdar, M., Sánchez-Ortiga, E., Martínez-Corral, M. & Javidi, B. Stable and simple quantitative phase-contrast imaging by Fresnel biprism. *Appl Phys Lett* 112, 1–5 (2018).
- 11. Chhaniwal, V., Singh, A. S. G., Leitgeb, R. A., Javidi, B. & Anand, A. Quantitative phase-contrast imaging with compact digital holographic microscope employing Lloyd's mirror. Opt Lett 37, 5127–5129 (2012).
- Trusiak, M., Picazo-Bueno, J. A., Patorski, K., Zdankowski, P. & Micó, V. Single-shot two-frame π-shifted spatially multi-plexed interference phase microscopy. J Biomed Opt 24(9), 096004 (2019).
- 13. Picazo-Bueno, J. A., Trusiak, M., García, J. & Micó, V. Spatially multiplexed interferometric microscopy: Principles and applications to biomedical imaging. *J Phys Photon* 3(3), 034005 (2021).
- 14. Tearney, G. J. & Yang, C. Wavefront image sensor chip. Opt Express 18, 16685-16701 (2010).
- 15. Kemper, B., Vollmer, A., Rommel, C. E., Schnekenburger, J. & von Bally, G. Simplified approach for quantitative digital holographic phase contrast imaging of living cells. *J Biomed Opt* 16, 026014 (2011).
- 16. Shaked, N. T. Quantitative phase microscopy of biological samples using a portable interferometer. Opt Lett 37, 2016–2018 (2012).
- 17. Lee, K. & Park, Y. Quantitative phase imaging unit. Opt Lett 39, 3630-3633 (2014).
- Guo, R., Mirsky, S. K., Barnea, I., Dudaie, M. & Shaked, N. T. Quantitative phase imaging by wide-field interferometry with variable shearing distance uncoupled from the off-axis angle. Opt Express 28, 5617–5628 (2020).
- 19. Li, Y. et al. Quantitative phase microscopy for cellular dynamics based on transport of intensity equation. Opt Express 26, 586–593 (2018).
- 20. Picazo-Bueno, J. A. & Micó, V. Optical module for single-shot quantitative phase imaging based on transport of intensity equation with field of view multiplexing. *Opt Express* **29**, 39904–39919 (2021).
- 21. Bhaduri, B. et al. Diffraction phase microscopy: Principles and applications in materials and life sciences. Adv Opt Photon 6, 57–119 (2014).
- 22. Picazo-Bueno, J. A., Trusiak, M. & Micó, V. Single-shot slightly off-axis digital holographic microscopy with add-on module based on beamsplitter cube. *Opt Express* 27, 5655–5669 (2019).
- 23. Trusiak, M. et al. Variational Hilbert quantitative phase imaging. Sci Rep 10(1), 13955 (2020).
- 24. Gabor, D. A new microscopic principle. Nature 161, 777-778 (1948).
- 25. Kreis, T. Handbook of Holographic Interferometry: Optical and Digital Methods (Wiley, 2005).
- 26. Micó, V., García, J., Zalevsky, Z. & Javidi, B. Phase-shifting Gabor holography. Opt Lett 34, 1492-1494 (2009).
- 27. Micó, V., García, J., Zalevsky, Z. & Javidi, B. Phase-shifting Gabor holographic microscopy. J Display Technol 6, 484-489 (2010).
- 28. Mandula, O. et al. Phase from defocus in quantitative phase imaging IV. In *International Society for Optics and Photonics* Vol. 10503 (eds Popescu, G. & Park, Y.) 112–123 (SPIE, 2018).
- 29. Mandula, O. *et al.* Phase and fluorescence imaging with a surprisingly simple microscope based on chromatic aberration. *Opt Express* **28**, 2079–2090 (2020).
- 30. de Kernier, I. *et al.* Large field-of-view phase and fluorescence mesoscope with microscopic resolution. *J Biomed Opt* **24**(03), 1–9 (2019).
- 31. Micó, V., Trindade, K. & Picazo-Bueno, J. A. Phase imaging microscopy under the Gabor regime in a minimally modified regular bright-field microscope. *Opt Express* **29**, 42738–42750 (2021).
- 32. Gerchberg, R. W. A practical algorithm for the determination of phase from image and diffraction plane pictures. *Optik* **35**, 237–246 (1972).
- 33. Fienup, J. R. Phase retrieval algorithms: A comparison. Appl Opt 21, 2758-2769 (1982).
- 34. Noom, D. W. E., Eikema, K. S. E. & Witte, S. Lensless phase contrast microscopy based on multiwavelength Fresnel diffraction. *Opt Lett* **39**, 193–196 (2014).
- 35. Noom, D. W. E., Flaes, D. E. B., Labordus, E., Eikema, K. S. E. & Witte, S. High-speed multi-wavelength Fresnel diffraction imaging. *Opt Express* 22, 30504–30511 (2014).
- 36. Sanz, M., Picazo-Bueno, J. A., Granero, L., García, J. & Micó, V. Compact, cost-effective and field-portable microscope prototype based on MISHELF microscopy. *Sci Rep* 7, 43291 (2017).
- 37. Sanz, M., Picazo-Bueno, J. A., García, J. & Micó, V. Improved quantitative phase imaging in lensless microscopy by single-shot multi-wavelength illumination using a fast convergence algorithm. *Opt Express* 23, 21352–21365 (2015).
- 38. Sanz, M., Picazo-Bueno, J. A., García, J. & Micó, V. Dual-mode holographic microscopy imaging platform. *Lab Chip* **18**, 1105–1112
- 39. Sanz, M., Picazo-Bueno, J. A., Granero, L., García, J. & Micó, V. Four channels multi-illumination single-holographic-exposure lensless Fresnel (MISHELF) microscopy. Opt Lasers Eng 110, 341–347 (2018).
- 40. Kazemzadeh, F. et al. Lens-free spectral light-field fusion microscopy for contrast- and resolution-enhanced imag-ing of biological specimens. Opt Lett 40, 3862–3865 (2015).
- 41. Liu, J. et al. Robust autofocusing method for multi-wavelength lensless imaging. Opt Express 27, 23814–23829 (2019).
- 42. Guo, C. et al. High-quality multi-wavelength lensfree microscopy based on nonlinear optimization. Opt Lasers Eng 137, 106402 (2021).
- 43. Luo, W., Zhang, Y., Feizi, A., Gorocs, Z. & Ozcan, A. Pixel super-resolution using wavelength scanning. *Light Sci Appl* 5(4), e16060 (2016).
- 44. Liu, Y. et al. Single-exposure multi-wavelength diffraction imaging with blazed grating. Opt Lett 47, 485-488 (2022).
- 45. Zuo, C., Sun, J., Zhang, J., Hu, Y. & Chen, Q. Lensless phase microscopy and diffraction tomography with multi-angle and multi-wavelength illuminations using a LED matrix. *Opt Express* 23, 14314–14328 (2015).
- 46. Waller, L., Kou, S. S., Sheppard, C. J. R. & Barbastathis, G. Phase from chromatic aberrations. Opt Express 18, 22817–22825 (2010).
- 47. Goodman, J. W. Introduction to Fourier Optics (Roberts & Company Publishers, 2005).

- 48. Xu, W. B., Jericho, M. H., Mcinertzhagen, I. A. & Kreuzer, H. J. Digital in-line holography for biological applications. *Proc Natl Acad Sci USA* 98, 11301–11305 (2001).
- Wu, Y. & Ozcan, A. Lensless digital holographic microscopy and its applications in biomedicine and environmental monitoring. *Methods* 136, 4–16 (2018).

Acknowledgements

V.M. and J.A.P.B. acknowledge grant PID2020-120056GB-C21 funded by MCIN/AEI/10.13039/501100011033. M.R. and M.T. acknowledge funding from National Science Center, Poland (2020/39/D/ST7/03236). Scientific Council for the Discipline of Automatic Control, Electronics, and Electrical Engineering (Warsaw University of Technology).

Author contributions

Conceptualization was performed by V.M., J.A.P.B. and M.T.; methodology was created by V.M., M.R. and M.T.; algorithm was designed by M.R. and M.T.; experiments were conducted by V.M. and J.A.P.B.; resources were granted by V.M. and M.T.; data curation was done by M.R., M.T. and V.M.; writing and original draft preparation were done by V.M. and M.R. and final version was refined by all coauthors. All authors have given approval to the final version of the manuscript.

Competing interests

The authors declare no competing interests.

Additional information

Supplementary Information The online version contains supplementary material available at https://doi.org/10.1038/s41598-023-31300-9.

Correspondence and requests for materials should be addressed to V.M.

Reprints and permissions information is available at www.nature.com/reprints.

Publisher's note Springer Nature remains neutral with regard to jurisdictional claims in published maps and institutional affiliations.

Open Access This article is licensed under a Creative Commons Attribution 4.0 International License, which permits use, sharing, adaptation, distribution and reproduction in any medium or format, as long as you give appropriate credit to the original author(s) and the source, provide a link to the Creative Commons licence, and indicate if changes were made. The images or other third party material in this article are included in the article's Creative Commons licence, unless indicated otherwise in a credit line to the material. If material is not included in the article's Creative Commons licence and your intended use is not permitted by statutory regulation or exceeds the permitted use, you will need to obtain permission directly from the copyright holder. To view a copy of this licence, visit http://creativecommons.org/licenses/by/4.0/.

© The Author(s) 2023